Materials Characterization 176 (2021) 111073

Contents lists available at ScienceDirect

Materials Characterization

journal homepage: www.elsevier.com/locate/matchar

On the microstructural origins of improvements in conductivity by heavy deformation and ageing of Al-Mg-Si alloy 6101

Jonas K. Sunde [a], Calin D. Marioara [b], Sigurd Wenner [b], Randi Holmestad [a,*]

[a] Department of Physics, Norwegian University of Science and Technology (NTNU), N-7491 Trondheim, Norway
[b] Materials and Nanotechnology, SINTEF Industry, N-7465 Trondheim, Norway

ARTICLE INFO

Keywords:
6xxx Al alloys
Electrical conductivity
Thermomechanical processing
Transmission electron microscopy
Atom probe tomography

ABSTRACT

This work has examined an Al-0.54Mg-0.38Si (at.%) conductor alloy (6101) subjected to two different thermomechanical processing routes. Conventional solution treatment, quenching, and artificial ageing (170 °C) was compared to a process applying solution treatment, quenching, pre-ageing (7 h at 170 °C), 50% thickness reduction by cold-rolling, and re-ageing at 170 °C. Re-ageing after rolling caused a rapid increase in electrical conductivity. After 2 h re-ageing the rate of change in conductivity had slowed to a level comparable to that of the undeformed material after the same total ageing time. From this point on the deformed material maintained a 2–3%IACS gain in conductivity with further ageing. It is shown that the improvement in conductivity could largely be explained by two precipitate formation mechanisms, leading to increased solute depletion of the Al matrix in the deformed material, which was quantified by atom probe tomography. Clear differences between the deformed and undeformed material were also seen in precipitate distributions as shown by transmission electron microscopy results. The findings and the discussion presented are of importance to future alloy and process development for Al alloy conductor materials.

1. Introduction

Al and its alloys are widely applied as conductor materials in e.g. land cables and overhead lines due to their high electrical conductivity-to-weight ratios and high specific strengths [1]. The industrial sector is in continuously growing demand for materials that can combine properties such as high strength, high electrical conductivity, low weight, and good corrosion resistance. The 6xxx series Al-Mg-Si alloys are among the top candidates, and are characterised by medium strengthening potential, good conductivity, and overall good forming and corrosion properties. As an example, Al-Mg-Si alloys are being developed for use in future subsea/offshore electrical cables.

One of the key challenges in further improving Al-Mg-Si alloys for conductor applications is to better optimise for high electrical conductivity while maintaining good mechanical performance. The problem is that the main factors that cause improvements in strength, including alloying (solid solution strengthening and precipitate strengthening) and deformation (reduction of grain size and work hardening), will lead to losses in electrical conductivity when compared to pure, undeformed Al. The development of alloys and thermomechanical processing (TMP) routines that can obtain better combinations of strength and conductivity depends on novel and clever approaches to alloy design [2–4].

For 6xxx series Al alloys in conductor applications, the combined alloying addition of Mg and Si is typically less than 1.6 at.%, e.g. 6101 and 6201 type alloys. The low addition of solutes means that these alloys can reach relatively high conductivities, combined with a medium level of strength. The strengthening is primarily caused by nano-sized precipitate phases that form during thermal ageing. The precipitates are needle- or rod-shaped, with main growth axis in $\langle 100 \rangle_{Al}$ directions. The types of precipitates that form, their sizes, and their dispersion in the Al matrix, all depend on alloy composition and TMP parameters. The precipitation sequence for the Al-Mg-Si system is normally stated as [5,6]:

$$\begin{aligned} &\text{SSSS} \rightarrow \text{solute clusters} \rightarrow \text{GP} - \text{zones} \left(\text{pre} - \beta^{''}\right) \\ &\quad \rightarrow \beta^{''} \rightarrow \beta^{'}, \text{U1}, \text{U2}, \text{B}^{'} \rightarrow \beta, \text{Si}. \end{aligned}$$

Here, SSSS denotes a supersaturated solid solution. For details on the different precipitate phase crystal structures, the following works should be consulted [7–12].

Several previous studies have demonstrated how different TMP

* Corresponding author.
E-mail address: randi.holmestad@ntnu.no (R. Holmestad).

https://doi.org/10.1016/j.matchar.2021.111073
Received 12 January 2021; Received in revised form 22 March 2021; Accepted 28 March 2021
Available online 31 March 2021

routes may yield good combinations of mechanical and electrical properties in Al-Mg-Si alloys, including processing by severe plastic deformation (SPD) [4,13,14], hydrostatic extrusion [15], drawing [16], and rolling [17,18]. A TMP route applying cold-rolling has been used in this work. The focus of the present study has been to advance the understanding of the microstructural origins of improvements in conductivity. This has been done by studying a 6101 Al alloy subjected to two different TMP routes, with conductivity and hardness measured as a function of ageing time. Microstructure characterisation was obtained by transmission electron microscopy (TEM) and atom probe tomography (APT). This provided detailed information on precipitate sizes and distributions, in addition to quantifying the matrix solute levels at different ageing conditions. The characterisation results were used to explain the differences obtained in material properties after equal ageing times for the two TMP routes. Such improvements in the understanding of how new TMP approaches affect microstructure-property relationships is a prerequisite for making yet further improvements in alloy design.

2. Methods

2.1. Material processing and property measurements

The studied 6101 Al alloy was manufactured by Hydro and was produced by rod-casting (Ø30 mm). The cast rods were subsequently cold-rolled to Ø15 mm. The alloy composition was measured by inductively coupled plasma optical emission spectroscopy (ICP-OES), and is shown in Table 1. The material was solution heat treated (SHT) at 530 °C for 20 min and then water quenched to room temperature. It was kept at room temperature (RT) for 15 min before it was set to artificial ageing (AA) in an oil bath conducted at 170 °C. In the following, this will be referred to as the undeformed material. In addition, another process was applied comprising solution treatment, quenching, pre-ageing (PA; 7 h at 170 °C), quenching, 50% thickness reduction by cold-rolling (50% CR), and subsequent re-ageing at 170 °C. This is denoted as the deformed material. A schematic of the two heat treatment procedures is provided in Fig. 1.

Hardness and conductivity measurements were performed after a series of holding times from 30 min to 4 days ageing, which spanned underaged (UA) to overaged (OA) material conditions. Vickers hardness (HV) tests were carried out on a Leica VMHT MOT hardness tester using a load of 1 kg and 10 s dwell time. 10 measurements were performed for each calculated average value. Conductivity was measured using a Foerster Sigmatester 2.069, and each value was determined as the average of 5 measurements.

2.2. TEM and APT experiments

Both TEM and APT specimens were prepared by standard electropolishing techniques, in addition to one APT specimen being prepared by focused ion beam milling. TEM specimens were obtained using a Struers Tenupol-5 twin-jet polishing unit with an electrolytic solution consisting of methanol (2/3) and nitric acid (1/3) held at −25 °C. APT specimens were obtained using three stages of thinning with gradually more reduced concentration of perchloric acid in the electrolyte mixture, see e.g. [19].

A JEOL 2100 microscope operated at 200 kV and equipped with a Gatan imaging filter was used for acquiring images for the calculation of precipitate statistics. The specimen thickness was measured by electron energy loss spectroscopy using the t/λ (log-ratio) method. Precipitate number density, N, length, l, cross-section area, a, and volume fraction, V_f, were obtained using established methodologies in microstructure quantification of Al alloys by TEM [20]. The precipitate number density was calculated as $N = 3N_{\parallel}/\left(A\left(t+\bar{l}_m\right)\right)$, where $N_{\parallel}$ is the number of precipitates oriented parallel to the beam direction, A is the area covered by the image, t is the specimen thickness in the image centre, and $\bar{l}_m$ is the average measured precipitate length. The volume fraction of precipitates was calculated as $V_f = N \cdot l \cdot a$. Energy dispersive spectroscopy (EDS) was performed on a JEOL 2100F microscope operated at 200 kV and equipped with an Oxford Instruments silicon drift detector and INCA software, used in analytical STEM mode with 1.5 nm probe size and step size of approximately 3 nm. Atomic resolution high-angle annular dark-field scanning TEM (HAADF-STEM) images were obtained on a double corrected JEOL ARM 200F microscope operated at 200 kV using a detector collection angle of 42–178 mrad.

APT experiments were performed using a Cameca LEAP 5000XS system. One specimen condition was field evaporated using electric pulses with a 333 kHz pulse repetition rate and 20% pulse fraction, and a specimen temperature of 40 K. Laser mode was used for three material conditions, using a pulse energy of 40 pJ and a pulse frequency of 500 kHz, conducted at 40 K. After reconstructing the background subtracted APT analysis volumes using the IVAS software, the precipitate phases were selected using Mg isosurfaces (normally 2 at.% Mg concentration). Precipitate compositions were subsequently obtained using the proxigram method. The matrix solute level was estimated from a cylinder that excluded the APT analysis volume edges (nodes) and precipitate volumes.

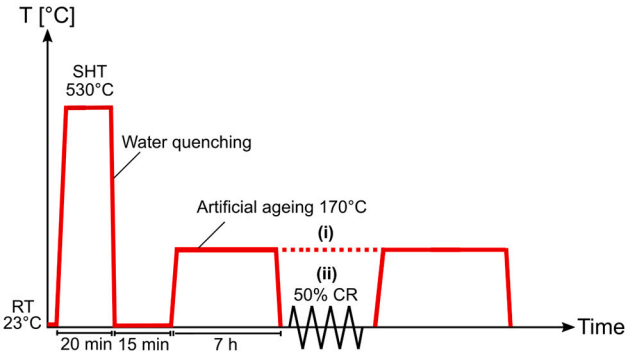

Fig. 1. The two heat treatment procedures applied for the studied Al-Mg-Si alloy. (i) Conventional SHT, water quenching, and AA. (ii) SHT, water quenching, PA (7 h at 170 °C), water quenching, 50%CR, and re-ageing at 170 °C.

Table 1
Composition of Al alloy 6101 as measured by ICP-OES. All other element concentrations were <0.005 at.%.

Alloy 6101	Al	Mg	Si	Fe
at./wt.%	bal.	0.54/0.50	0.38/0.41	0.05/0.10

3. Results

3.1. Material properties

The obtained material hardness and electrical conductivity after different ageing times are shown in Fig. 2. It is seen that the 7 h ageing condition, which was selected as the PA treatment, corresponded to an UA condition with a hardness of ≈ 74 HV. After 50%CR reduction it is seen a significant increase (ΔHV ≈ 21) in material hardness as compared to the (undeformed) PA condition, reaching approximately 95 HV in the as-deformed condition. This was higher than the maximum hardness obtained with isothermal ageing at 170 °C, which reached about 85 HV after 24 h ageing. In the start of re-ageing, the as-deformed material showed large changes in material hardness. At 10 h accumulated ageing (7 h PA + 3 h re-ageing), the hardness of the deformed material measured 90.0 ± 2.1 HV, and beyond this point it gradually decreased with further ageing. At 15 h ageing the hardness of the deformed and undeformed materials were nearly equal at ≈ 80 HV.

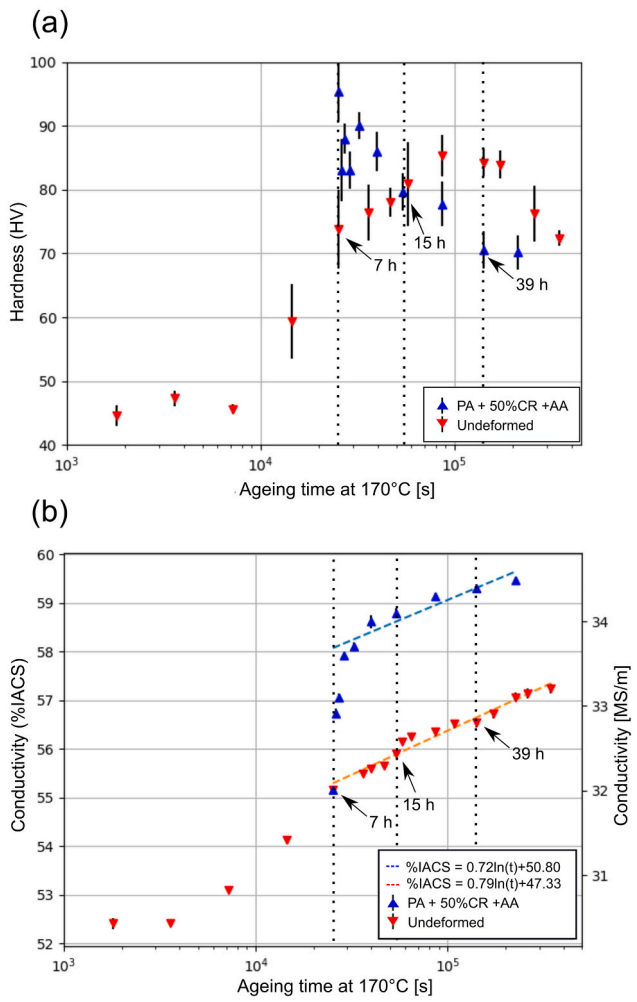

Fig. 2. (a) Vickers hardness and (b) electrical conductivity measured for the deformed and undeformed materials after different ageing times at 170 °C. The conductivity data after >9 h ageing at 170 °C have been fitted using logarithmic functions of time, t [s].

The conductivity of the as-deformed condition was nearly unchanged relative to the 7 h undeformed ageing condition (PA step), both at about 55%IACS (% of the international annealed copper standard which equals 58 MS/m). Upon re-ageing, the as-deformed material showed a sharp increase in conductivity, from 7 h (deformation stage) to 9 h ageing. Here, the conductivity increased from 55.2%IACS to 58.1% IACS. After the 9 h total ageing condition, the slope of the conductivity curves were nearly equal for the deformed and undeformed materials, as seen from the fitted lines in Fig. 2b. At >9 h ageing the conductivities of the deformed and undeformed materials maintained a difference of $\Delta\sigma \gtrsim$ 2.1%IACS, being higher in the former. Based on the obtained hardness and conductivity measurements, six conditions were selected for microstructure characterisation, see Table 2.

Table 2
Ageing conditions selected for microstructure characterisation and the corresponding material properties.

Ageing condition	Hardness HV	Conductivity MS/m / %IACS
7 h undef.	73.8 ± 6.2	32.0 ± 0.1 / 55.2 ± 0.2
15 h undef.	80.9 ± 6.5	32.4 ± 0.1 / 55.9 ± 0.2
39 h undef.	84.2 ± 2.2	32.8 ± 0.1 / 56.6 ± 0.2
7 h def.	95.4 ± 4.8	32.0 ± 0.1 / 55.2 ± 0.2
15 h def.	79.7 ± 2.9	34.1 ± 0.1 / 58.8 ± 0.2
39 h def.	70.6 ± 2.9	34.4 ± 0.1 / 59.3 ± 0.2

3.2. Microstructure observations by TEM

3.2.1. Undeformed material

From left to right, Fig. 3 shows TEM images of alloy 6101 undeformed after 7 h, 15 h, and 39 h isothermal ageing at 170 °C, respectively. Based on a series of bright-field (BF) TEM images used to measure precipitate length distributions (e.g. Fig. 3a-c) and cross-sections (e.g. Fig. 3d-f), the precipitate statistics in these conditions were calculated, see Table 3. At 7 h ageing it is seen a dense distribution of relatively short precipitates, mostly confined to the range 5–30 nm in length. From the HAADF-STEM lattice images (Fig. 3g,h,m,n) it is seen that the precipitates were predominantly β'' phase [7], albeit some with fragments from other Al-Mg-Si phases, such as B′ (Fig. 3h) [11] and β' (Fig. 3n) [8]. At 15 h ageing it is seen from Table 3 that there has occurred a significant drop in the precipitate number density, from 20881 ± 2162 μm^{-3} to 13861 ± 1499 μm^{-3}, obtained at 7 h and 15 h ageing, respectively. This is also qualitatively indicated from a comparison of images Fig. 3a and Fig. 3b, acquired at comparable thicknesses, where the distribution in Fig. 3b is less dense. HAADF-STEM lattice images (Fig. 3i,j,o,p) at 15 h ageing showed that β'' was still the dominant phase, and generally with larger cross-section areas than for the 7 h condition. Fig. 3j shows an example of a near 50/50 β''/β' precipitate, with a sharp and well-defined interface between the two phases. As seen from the hardness plot in Fig. 2a, the hardness increases from the 7 h to the 15 h condition. The precipitates have increased in size, the number density has decreased, and the volume fraction of precipitates has increased, indicating coarsening of precipitates and a continued solute uptake in precipitate structures, see Table 3.

After 39 h ageing, it is seen from Fig. 3c that some precipitates had grown very long as compared to previous conditions, with several of them exceeding 100 nm in length. On closer observation, it is also seen that there existed a relatively high density of shorter precipitates, which is also seen from Fig. 3f. For the measured precipitate lengths at the 39 h ageing condition it was also seen a two-fold length distribution (not shown). HAADF-STEM lattice images (Fig. 3k,l,q,r) at 39 h ageing showed that large β'' phases were still present, but now pure post-β'' precipitates could also be seen, e.g. β' (Fig. 3r). Fig. 3l shows another example of a near 50/50 β''/β' precipitate. The calculated volume fraction was higher than for the 15 h condition, calculated as 0.82 ± 0.10% compared to 0.68 ± 0.09% for the 39 h and 15 h conditions, respectively. The 39 h condition is at the peak hardness plateau as seen from Fig. 2a, prior to the onset of overageing. More surprisingly, the calculated number density (20033 ± 2093 μm^{-3}) is seen to be higher than the 15 h condition (see Table 3), and is similar to the 7 h condition. The measurements for the 39 h condition were repeated using a different specimen, which also gave a similar result. This indicated that there was a re-precipitation occurring in-between the 15 h and 39 h ageing conditions. Re-precipitation is here interpreted as occurring due to some coarser precipitate structures being dissolved (at least partially), with new atomic clusters/GP-zones forming from the released solutes. Subsequently, these grow to form precipitates in higher densities than would occur without dissolution of large precipitates.

3.2.2. Deformed material

Fig. 4 shows BF and dark-field (DF) TEM images of the deformed material (PA + 50%CR + AA) in the three studied ageing conditions. The high degree of deformation introduced in the 50%CR stage is clearly visible in all images, showing a dense network of dislocations. In the as-deformed condition (Fig. 4a,d) it was difficult to discern any precipitates, in both BF and DF images, and long exposure selected area diffraction patterns did not reveal their presence (Fig. 4d). This indicated that the precipitate crystal structures have been disrupted by the CR process, either partially or completely. Gradual disruption of β'' crystal structures has also been observed in pre-aged specimens compressed to different degrees [21], and is caused by precipitates being repeatedly sheared by moving dislocations. It has also been observed

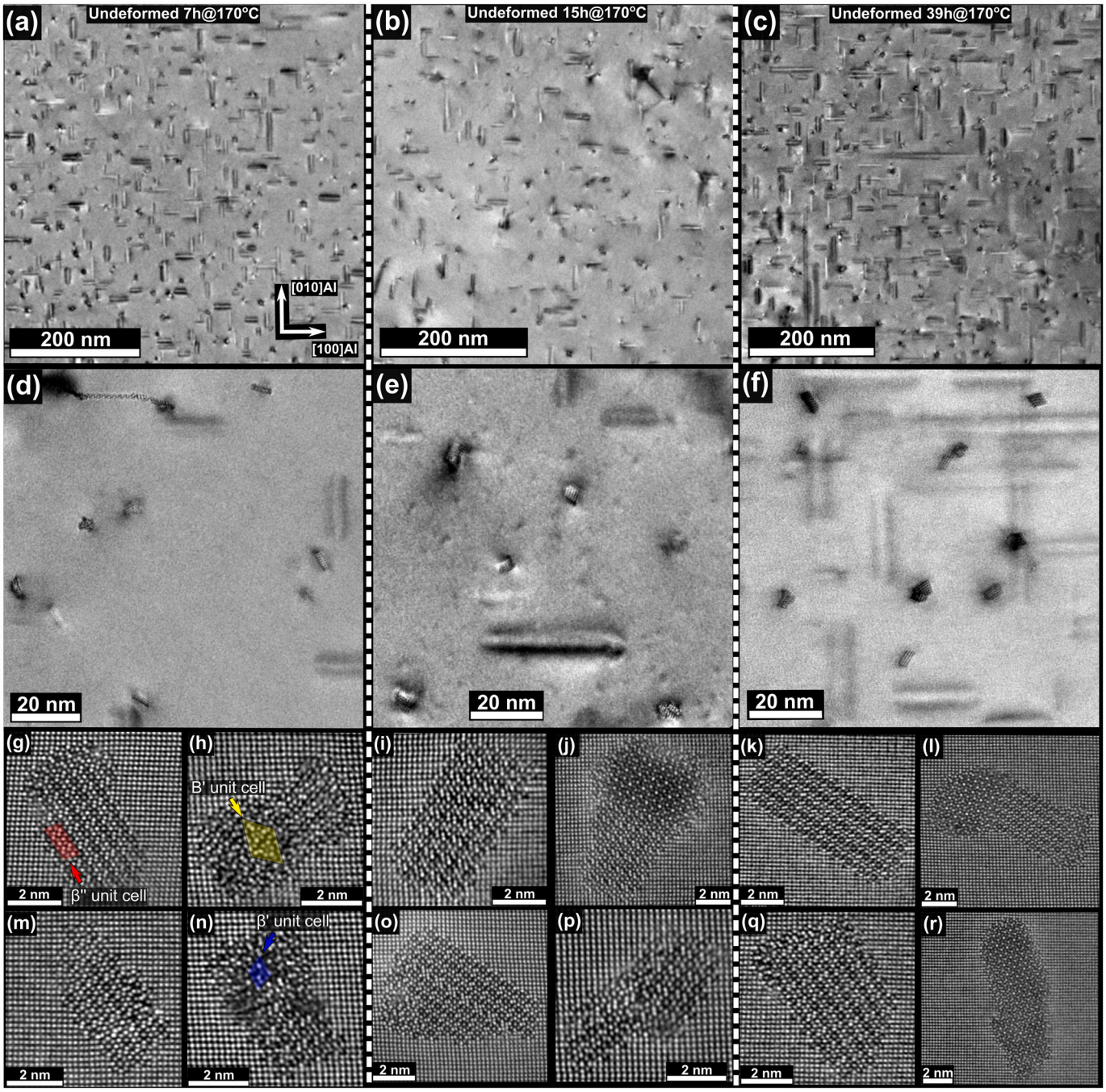

Fig. 3. From left to right: TEM images of Al alloy 6101 at indicated isothermal ageing conditions in the undeformed material. (a-f) BF TEM images showing precipitate lengths and cross-sections and (g-r) HAADF-STEM lattice images showing representative precipitate structures from each ageing condition. All images are acquired close to the $[001]_{Al}$ zone axis.

Table 3
Calculated precipitate statistics for alloy 6101 in the undeformed ageing conditions studied.

Ageing condition	Cross-section area [nm^2]	Precipitate length [nm]	Precipitate density [μm^{-3}]	Volume fraction [%]
7 h undef.	12.5±0.5	20.6±0.4	20881±2162	0.54±0.06
15 h undef.	14.5±0.4	33.8±1.0	13861±1499	0.68±0.09
39 h undef.	14.0±0.4	29.3±0.8	20033±2093	0.82±0.10

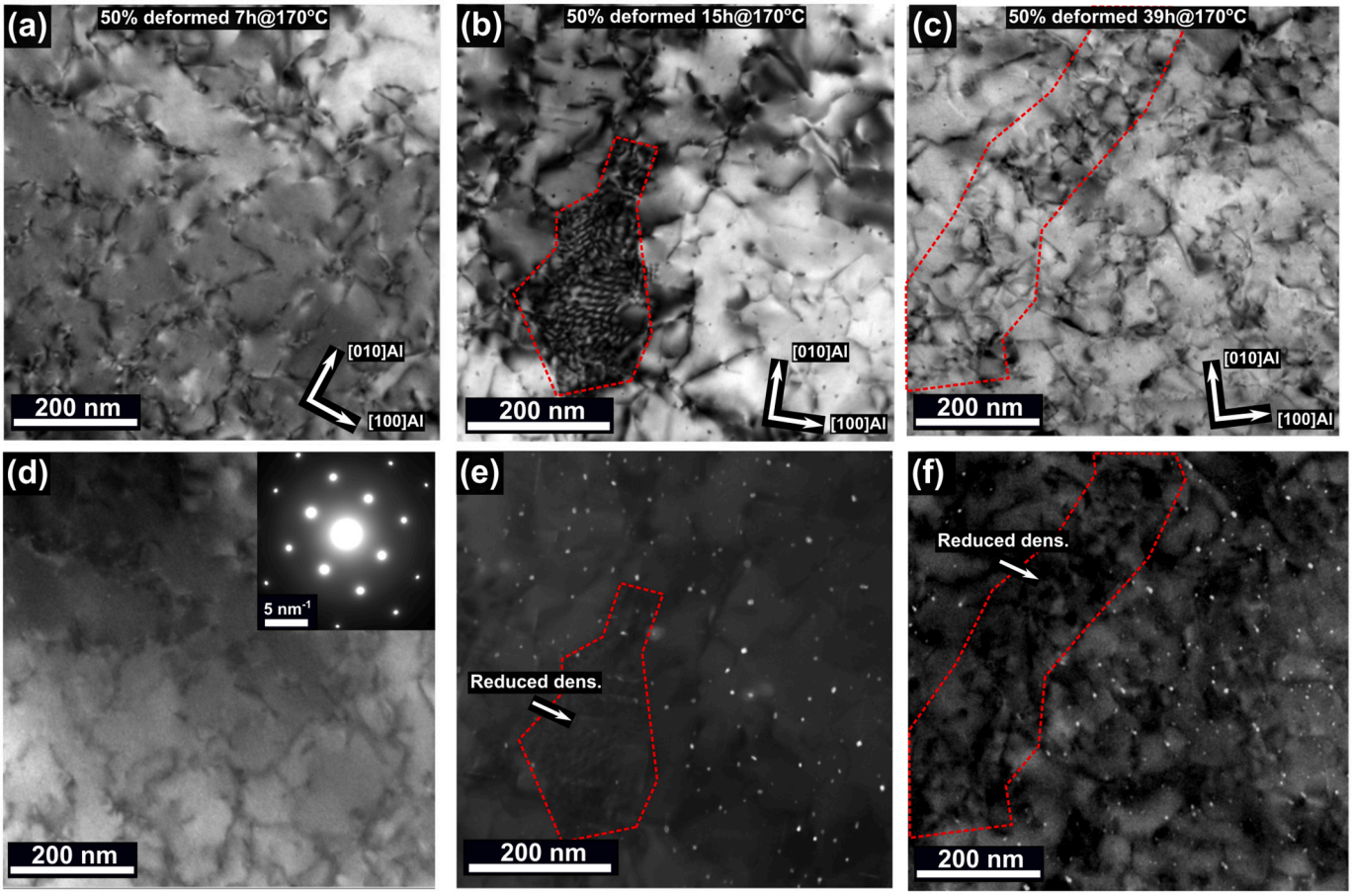

Fig. 4. BF (a-c) and corresponding DF (d-f) TEM images acquired in the deformed 6101 alloy after (a,d) 7 h (as-deformed), (b,e) 15 h, and (c,f) 39 h ageing at 170 °C, respectively. The insert of image (d) shows a selected area diffraction pattern acquired in the imaged region. Highlighted areas (red) indicate regions of reduced precipitate density. All images are acquired close to the $[001]_{Al}$ zone axis. (For interpretation of the references to colour in this figure legend, the reader is referred to the web version of this article.)

previously in the study of a 6101 Al alloy subjected to 70%CR [18].

After 15 h ageing (PA + 50%CR + 8 h re-ageing), there were clear observations of precipitates present, see Fig. 4e. From a series of corresponding BF/DF images as the ones shown in Fig. 4 there were indications of reduced precipitate density in regions that seemed to have a particularly high dislocation density, as exemplified by the highlighted regions in Fig. 4b,e. This reduced precipitate density in regions of high dislocation density was also found for the 39 h deformed ageing condition, see Fig. 4c,f. Qualitatively, the overall precipitate density at the 39 h deformed condition seemed lower than the 15 h deformed condition.

Due to the heavy deformation it was difficult to obtain any quantitative precipitate statistics in the deformed conditions. One difference observed between the deformed and undeformed material conditions was that the precipitate distributions in the deformed conditions were more inhomogeneous than the corresponding undeformed conditions. Larger bands or regions with few or no precipitates were observed in the deformed material. Judging from the BF image contrast, these regions typically showed increased dislocation density or dislocation bands, similar to the region highlighted in Fig. 4c,f.

Fig. 5 shows ADF-STEM images and long exposure EDS mapping results of the deformed alloy conditions. For the as-deformed condition shown in Fig. 5a, it is observed from the EDS maps that there were some regions locally richer in Si and Mg (highlighted), although the signal is weak. This could indicate that GP-zones and/or precipitates were still present after deformation, which was not observed using BF/DF imaging and selected area diffraction.

As expected for the 15 h deformed condition the EDS maps show that there were precipitates present, and the $\langle 001 \rangle_{Al}$ oriented needle morphology as observed close to the $[001]_{Al}$ zone axis is readily seen from the Si and Mg maps, see Fig. 5b. Furthermore, it is also observed extended regions of solute enrichment and depletion (highlighted), which correlate well with some of the main dislocation features observed in the ADF-STEM image in Fig. 5b. This clearly demonstrates that the introduced dislocations have a significant impact on the redistribution of solutes and the precipitation that takes place after re-ageing. These extended solute enriched regions indicate either a continuous precipitation along the dislocation lines, or a combined precipitation and solute segregation.

At the 39 h deformed condition (Fig. 5c) there were also similar observations of precipitate distributions having been affected by the dislocation microstructure. This is for instance seen from the highlighted line of continuous precipitation, with depleted regions on either side. Qualitatively, the overall precipitate density seemed significantly lower than the 15 h deformed condition, and in addition much more inhomogeneous. This was also observed in additional EDS maps acquired (not shown).

3.3. Assessment of solute levels by APT

APT experiments were performed on the 7 h undeformed and deformed conditions, as well as the 15 h undeformed and deformed conditions. One selected reconstructed analysis volume is shown for each of the 4 conditions in Fig. 6. The precipitate phases were isolated by

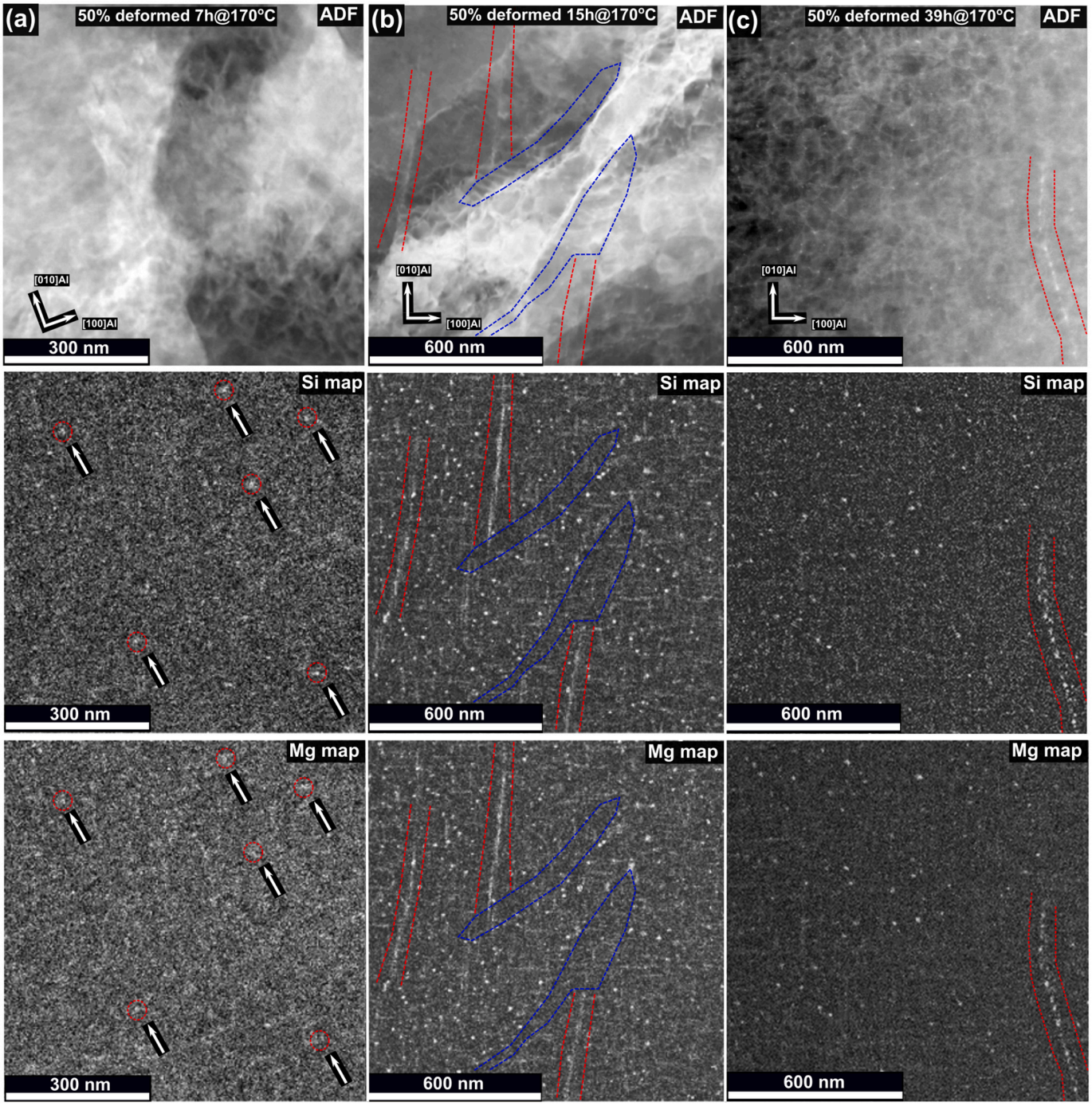

Fig. 5. ADF-STEM images and the corresponding Si and Mg EDS maps from the deformed 6101 alloy after (a) 7 h (as-deformed), (b) 15 h, and (c) 39 h total ageing at 170 °C, respectively. In the EDS maps of (a) there are corresponding regions with slightly increased Si and Mg concentration (albeit very weak), some of which are highlighted by arrows. The highlighted regions (red) in (b) and (c) show a central line rich in solutes and/or precipitates with adjacent solute depleted bands. Highlighted (blue) regions in (b) indicate regions more depleted of solutes/precipitates than average, and with no solute rich interior. All regions highlighted in (b) and (c) lie close to main dislocation features seen in the corresponding ADF-STEM images. All images/maps are acquired close to the $[001]_{Al}$ zone axis. (For interpretation of the references to colour in this figure legend, the reader is referred to the web version of this article.)

forming Mg and/or Si isosurfaces of ≈ 2 at.% concentration. It is seen that all volumes contain precipitates, including the 7 h as-deformed condition, see Fig. 6b. The observation of precipitates in the 7 h deformed condition is an important finding, which demonstrates that the precipitates may at least be partially preserved, even after 50%CR reduction. Several small and rounded precipitates/GP-zones were also present inside this volume. This was also observed for two additional APT datasets acquired in this condition (not shown). The reduced size and more spherical appearance of precipitates/GP-zones in the as-deformed condition as compared to the undeformed state, see Fig. 6a, indicate that the majority of precipitate structures has been significantly altered by the CR stage. The precipitate crystal structures have almost been completely destroyed by the repeated shearing caused by dislocations, which was also seen from TEM results, see section 3.2.2.

Having isolated the precipitate volumes, the average precipitate and matrix compositions were obtained. The results are summarised in

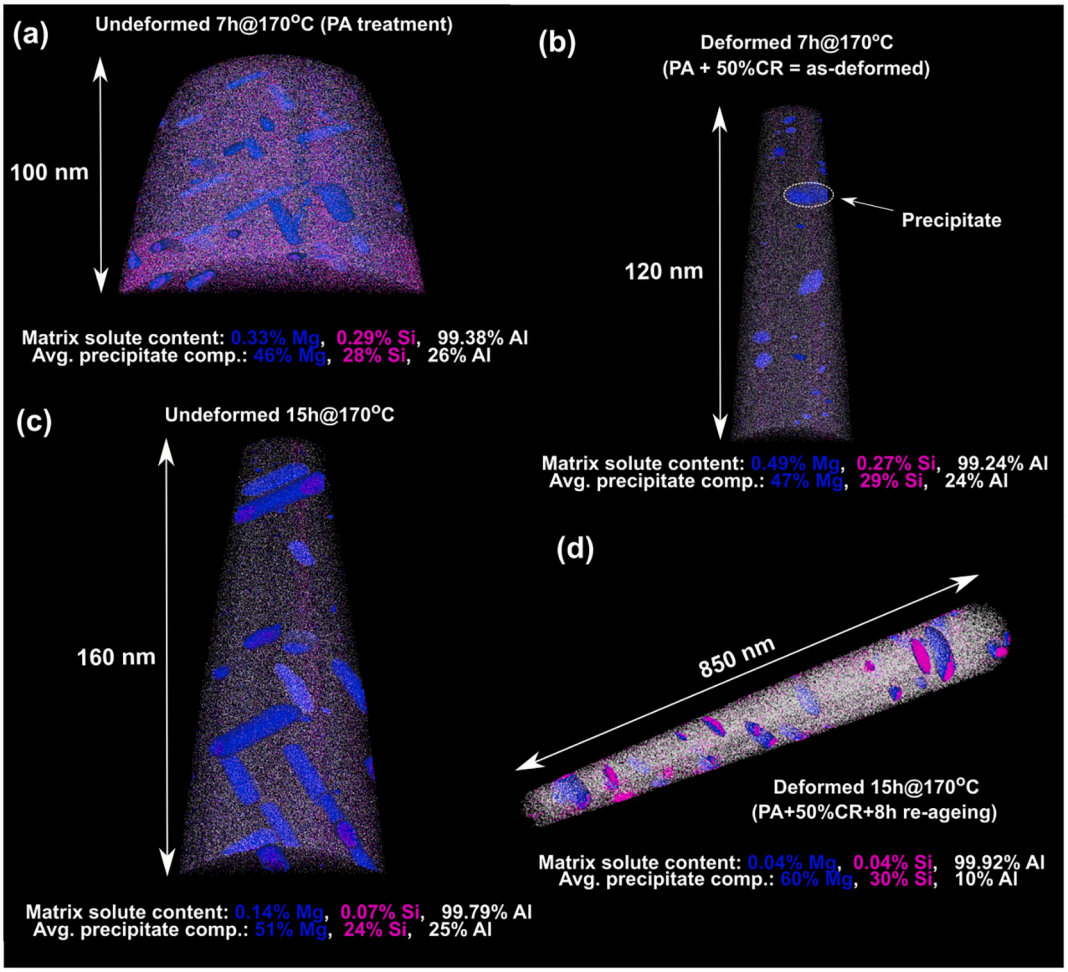

Fig. 6. Reconstructed APT volumes from indicated 6101 alloy conditions. Blue, pink, and white datapoints indicate respectively Mg, Si, and Al atoms. 2 at.% Mg isosurfaces (blue volumes) were typically used to isolate precipitate phases. (For interpretation of the references to colour in this figure legend, the reader is referred to the web version of this article.)

Table 4
Calculated average precipitate composition and the estimated solute concentration in the Al matrix obtained from APT results.

Ageing condition	Avg. precipitate composition [%]	Matrix solute levels [at. %]
7 h	46±2%Mg, 26±1%Al,	0.33±0.02Mg
Undeformed	28±1%Si	0.29±0.03Si
7 h	47±2%Mg, 24±2%Al,	0.49±0.02Mg
Deformed	29±2%Si	0.27±0.03Si
15 h	51±2%Mg, 25±2%Al,	0.14±0.01Mg
Undeformed	24±1%Si	0.07±0.02Si
15 h	60±2%Mg, 10±1%Al,	0.04±0.01Mg
Deformed	30±1%Si	0.04±0.02Si

Table 4. It is seen that the average precipitate composition in the 7 h undeformed condition corresponds with an UA condition when compared to the reported composition of the β'' phase, given as $Mg_5Al_2Si_4$ (45%Mg, 18%Al, 36%Si) [7]. UA precipitates are typically characterised by a high Al content. The matrix solute levels were measured as 0.33 Mg and 0.29 Si at.% which showed that there were significant amounts of solutes left in solid solution after the PA step, to be compared with the measured alloy composition: 0.54Mg-0.38Si at.%. A similar average precipitate composition to that of the 7 h undeformed material was also measured in the as-deformed condition. However, the matrix solute levels measured in the as-deformed condition differed from the undeformed material, particularly due to the increased levels of Mg, which was measured as 0.49 Mg at.%. This shows that a significant level of Mg has been reintroduced in the Al matrix during the 50%CR stage because of precipitate crystal structure disruption.

From the 7 h to the 15 h undeformed condition there occurred a coarsening and dissolution of precipitates, seen from the drop in precipitate number density and the increase in average precipitate size and volume fraction, see Table 3. In terms of material properties, there is a gain in alloy hardness of about 7 HV and 0.7%IACS in conductivity from the 7 h to 15 h stage, see Table 2. The APT matrix solute level measurements show a significant drop in the Mg and Si content, from 0.33 to 0.14 at.% Mg, and from 0.29 to 0.07 at.% Si, measured for the 7 h and the 15 h undeformed conditions, respectively.

In the 15 h deformed condition, it was measured a very low matrix solute content of Mg and Si, obtained as 0.04 at.% Mg and 0.04 at.% Si. This was also lower than the corresponding undeformed condition. These two conditions are at comparable hardness levels, obtained as 80.9 and 79.7 HV for the undeformed and deformed conditions, respectively (see Table 2). The conductivity of the deformed material was however significantly higher, at 58.8%IACS for the deformed condition compared to 55.9%IACS for the undeformed material. The difference of 2.9%IACS at similar hardness levels is an interesting finding. The APT data show support for the measured difference in electrical conductivity, due to the measurement of a lower matrix solute content in the deformed material.

When Al-Mg-Si alloys reach OA conditions, post-β'' precipitate phases such as β' ($Mg_6Si_{3.33}$) and eventually β (Mg_2Si) phase form, which are progressively more rich in Mg relative to Si [6]. This is reflected in the

composition of the precipitates in the 15 h deformed and undeformed conditions, as compared to the corresponding 7 h conditions. The precipitates in the 15 h undeformed condition still contain a high level of Al (25%), whereas the precipitates in the 15 h deformed condition contain only 10% Al. The precipitates of the 15 h deformed condition are therefore closest to the β' phase composition ($Mg_6Si_{3.33}$), and can therefore be said to be effectively more aged as compared to the precipitates in the 15 h undeformed material. This indicated that accelerated precipitation kinetics occurred in the deformed and re-aged material.

4. Discussion

4.1. Microstructural contributions to electrical resistivity

Matthiessen's rule is an empirical relation that expresses the total electrical resistivity of a crystalline metal, ρ_{tot}, as a linear sum of the individual contributions from different microstructural features in the metal. In Al alloys, there are several features in the microstructure that have an effect on the electrical resistivity. The total electrical resistivity, ρ_{tot}, as a function of temperature, T, and the matrix solid solution concentration of elements, c_i, may be stated as

$$\rho_{tot}(T, c_i) = \rho_0(T) + \sum_i \alpha_i c_i + \rho_{disloc} + \sum_j f_{par,j}\ \rho_{par,j} + \rho_{GB}. \quad (1)$$

Here, ρ_0 is the resistivity of pure aluminium. It contains among others the effect of phonons, and therefore has a strong temperature dependence. The conductivity measurements in this work were carried out at room temperature, where $\rho_0 = 2.655 \cdot 10^{-6}$ Ωcm. The factor $\rho_{par,\,j}$ accounts for the effect of precipitates (particles) in the microstructure, each with a volume fraction, $f_{par,\,j}$. The constants ρ_{disloc}, ρ_{GB}, and α_i account for the contribution of dislocations, grain boundaries, and solute elements in the Al matrix of a concentration c_i (wt.%), respectively. The element-specific coefficients α_i at 20 °C equal 0.6186 and 0.5745 Ω·cm/wt.% for Si and Mg, respectively [22,23]. This shows that the contributions to the electrical resistivity from the precipitate forming elements Mg and Si left in solid solution are nearly equal. This also explains why conductivity curves obtained for Al-Mg-Si alloys as a function of ageing time are generally continuously increasing. With ageing, progressively more solutes are locked inside precipitate phases, which increases the precipitate volume fraction, and gives less solute left in the Al matrix. Furthermore, the sensitivity to either element in solid solution is similar, which means that despite changes in average precipitate composition, the overall conductivity should generally increase.

The mean free path of conducting electrons in Al is $\lambda_{Al} = 14$ nm at room temperature [23]. When both the average precipitate dimensions and interparticle spacing are larger than this length, their contribution to electrical resistivity is relatively small. As the grain size of typical Al alloys is also much larger than this length, the factor ρ_{GB} is also negligible. In alloys processed by SPD, where average grain diameters can be on the order of 100 nm, the contribution can however be significant [4,13,14,24]. In terms of the dislocation contribution, ρ_{disloc}, Miyajama et al. [25] have shown good agreement with experimental findings using $\rho_{disloc} = 2.7 \cdot 10^{-25}$ Ωm^3. However, as seen from Fig. 2a, the conductivity of the studied material before and after 50%CR remained unchanged, and the dislocation contribution is therefore thought to be of second order here.

For the alloy conditions studied, the main contribution to the electrical resistivity is hence due to the solid solution term $\sum_i \alpha_i c_i$, with other terms in Eq. 1 being small in comparison. By comparing the 15 h deformed and undeformed ageing conditions, see Table 4, it is seen that the deformed material had a lower matrix solute content of Si and Mg, which supports the measurement of a higher conductivity for this condition, see Table 2. The differences in matrix solute levels between the deformed and undeformed 15 h conditions are 0.10 at.% Mg and 0.03 at.% Si. In order to form an idea of the effect such a difference in matrix solute levels might give, the resistivity is approximated as $\rho_{tot}(293\ \mathrm{K}, c_i) = 2.655 \cdot 10^{-6}\ \Omega\mathrm{cm} + \sum_i \alpha_i c_i$. This gives for the difference in conductivity $\Delta\sigma = 1/\rho_{15h,\ def} - 1/\rho_{15h,\ undef} \approx 1.8\%$IACS, obtained using the matrix solute levels measured by APT for the 15 h deformed and undeformed conditions given in Table 4. This is to be compared with the 2.9%IACS difference in conductivity measured between the 15 h deformed and undeformed ageing conditions, see Table 2. Despite the great simplifications made in this approximation, it still shows that the main cause of the difference in conductivity can be attributed to the change in matrix solute levels that develops during ageing of the deformed and undeformed materials. The deformation was also observed to have a significant effect on the precipitate distribution after re-ageing, e.g. by forming extended regions of solute depletion and continuous precipitation along dislocation lines, see Fig. **5**b,c. This non-uniform microstructure may also have an effect on the electrical conductivity, which is difficult to quantify.

4.2. On the rapid increase in conductivity after deformation

Re-ageing following 50%CR reduction caused a very sharp increase in conductivity, from 55.2%IACS to 58.1%IACS, in about 2 h ageing time at 170 °C, see Fig. 2b. In the 7 h undeformed ageing condition (PA treatment) there existed a relatively dense microstructure of primarily pure β'' precipitates, see **Fig. 3**, containing less than half of the total solute additions available in the alloy, see Table 4. By subsequently deforming the material in this UA condition, many precipitate-dislocation interactions will have occurred, leading to a dense and evenly distributed network of dislocations. The solute atoms, atomic clusters/GP-zones, and precipitates present in the matrix act as obstacles to the moving dislocations. The precipitates will have been sheared multiple times due to the high degree of deformation introduced, which will cause partial or complete disruption of the preciptiate crystal structures [21].

Due to the high strain rates involved in cold-rolling, and hence high dislocation velocities, solute segregation or formation of Cottrell atmospheres near moving dislocations will unlikely have occurred to any significant extent, as this is promoted at lower dislocation velocities [26]. Due to the large plastic deformation the dislocation microstructure will have developed into a highly complex and entangled network, where most dislocations have been pinned at multiple points on the different dislocation obstacles present in the 7 h ageing condition. The disruption of precipitate crystal structures was evident from microstructure observations after 50%CR (Fig. 4a,d), where the precipitates proved difficult to observe based on TEM imaging techniques utilising diffraction contrast (BF/DF). Long exposure EDS maps did however indicate that Mg and Si rich regions were still present, see Fig. 5a. This was confirmed by APT results, which showed that a high density of rounded precipitates/GP-zones was present after the deformation stage, see Fig. 6b.

Despite precipitate crystal structures being at least partially destroyed, the solutes are thought to remain relatively confined to their initial positions (prior to CR) due to the large dislocation velocities involved in cold-rolling. Moreover, the conductivity measured before and after 50%CR remained unchanged (see Fig. 2b). APT data showed that significant levels of Mg were released from precipitates in the CR process. The matrix solid solution level of Mg was measured as 0.33 at.% and 0.49 at.% for the 7 h undeformed and deformed conditions, respectively. If the difference of 0.16 at.% Mg was uniformly distributed in the Al matrix, it should have reduced the conductivity of the deformed material by a value similar to the calculated difference between the 15 h deformed and undeformed conditions ($\Delta\sigma \approx 1.8\%$IACS). This is taken as an indirect evidence showing that the position of solute rich regions present in the 7 h undeformed condition (GP-zones, precipitates, etc.), does not change significantly through the CR process. Instead, the distribution of solute rich regions is smeared out to some extent, which is supported by APT data. Because the overall distribution of solutes in the

microstructure does not change considerably between the 7 h undeformed and deformed conditions, the conductivity does not change significantly.

In the next step, this highly entangled dislocation microstructure, pinned on partially/completely disrupted precipitate crystal structures and solute enriched regions, is subjected to re-ageing at 170 °C. The high degree of deformation will have increased the concentration of vacancies in the material considerably [27,28], mainly due to vacancies being generated by moving jogs of screw dislocations. In this stage, it is envisioned two different main mechanisms taking place: (i) conventional bulk diffusion of solutes and resulting nucleation and growth away from the dislocation network, and (ii) rapid pipe (/dislocation) diffusion of solutes causing re-growth of locally solute enriched regions/partially disrupted precipitates pinning dislocations and new heterogeneous nucleation on dislocations. Both effects will have been enhanced by the increased vacancy levels introduced in the deformation stage. Similar ideas about the effect of dislocations on subsequent precipitation have been presented in other works, e.g. [29]. The dislocations will also be able to move and become unpinned, leading to dislocation recovery. The large changes in hardness seen from Fig. 2a immediately after deformation is a clear indication of this. Increase in hardness from (re-) precipitation and a reduction due to dislocation recovery is competing at this initial stage.

Bulk solute diffusion around a static dislocation is well-established in continuum models [30,31], which show that the Mg atoms will diffuse and bind to the tensile stress field of the dislocation due to its increased size misfit relative to Al atoms. This effect is well-known, particularly for Al-Mg alloys (5xxx), where it may manifest itself in the phenomena of dynamic strain ageing (DSA) and the Portevin-le Chatelier effect [30,31]. Si on the other hand, will bind to the compressive field of the dislocation due to its negative size misfit [32].

Fast diffusion of solutes along dislocation cores for different types of dislocations in Al has been treated and demonstrated previously [26,33–36]. For Mg, this has been treated extensively, in studies of aspects related to DSA [31,37]. For Si, the diffusion along a single dislocation line between silicon nano-precipitates in an Al thin film was studied in situ, showing that dislocations accelerate the diffusion of solutes by almost three orders of magnitude as compared to bulk diffusion [38]. Similar results have also been demonstrated previously, by indirect assessments [39]. Calorimetric studies of the dynamics of solute clustering have also suggested that solute migration takes place by pipe diffusion at early times and by bulk diffusion at later times during the clustering process [40].

The increased diffusivity of solute elements as enhanced by the aforementioned effects will cause a more rapid depletion of the matrix Mg and Si solute content in the deformed as compared to the undeformed material, and hence resulting in an increase in electrical conductivity. The APT and EDS data showing segregation of solutes and continuous precipitation along dislocations with adjacent solute depleted zones (see Fig. **5**b,c) support this hypothesis. The improvement in conductivity is therefore seen as a consequence of improved 'vacuuming' of the matrix solutes, leaving the conducting electrons with a path of least resistance through the matrix. Fig. 7 presents a schematic visualisation of the proposed microstructure evolution for the two TMP routes applied in this work.

After the initial rapid increase in conductivity upon re-ageing of the deformed material, the slope of the conductivity curves become nearly equal at >9 h ageing for the deformed and undeformed materials as seen from the fitted lines in Fig. 2b. This is interpreted as an indication that the pipe diffusion of elements along dislocations has halted for the deformed material, and the subsequent microstructural changes proceed as in conventional overageing, characterised by coarsening of larger precipitates and dissolution of smaller ones.

The findings have important implications in optimising for high conductivity while retaining high material strength. The largest increase in conductivity occurs shortly after re-ageing the as-deformed material. Rapid precipitation and dislocation recovery will occur concurrently, with an increasing conductivity and a gradually reduced material strength. A moderate re-ageing step applied after deformation of a pre-aged material should therefore lead to a good combination of high conductivity while retaining good material strength. Increasing the ageing temperature, using different modes and degrees of deformation,

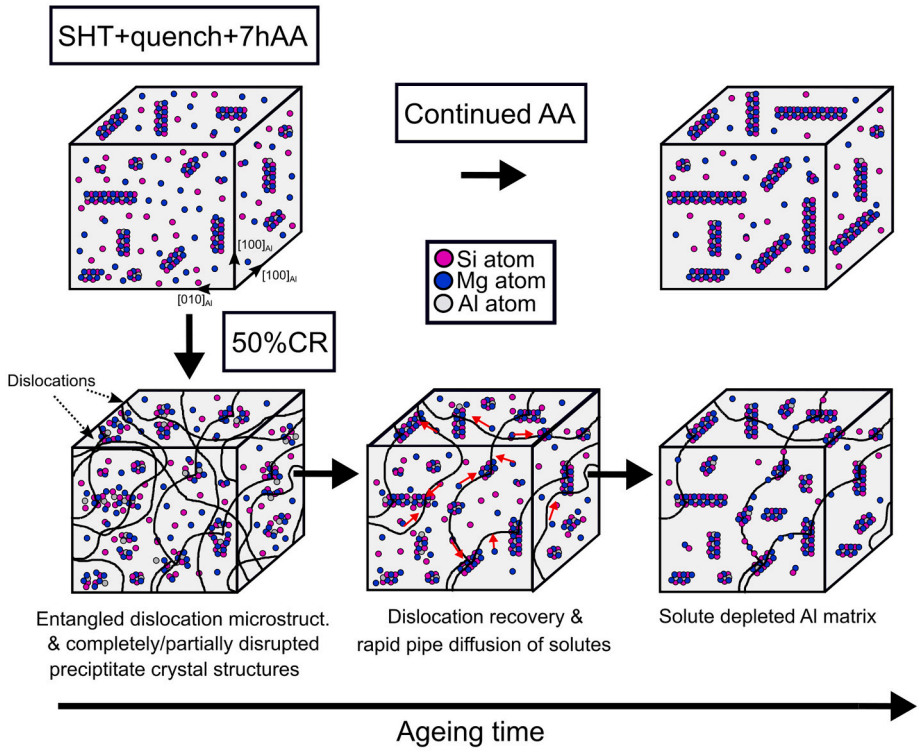

Fig. 7. Schematic representation of the microstructure evolution envisioned for the two TMP routes applied to the 6101 Al alloy studied in this work.

and/or applying different durations in the PA treatment are also parameters that should be explored more carefully in order to design optimum TMP routines for achieving good material property combinations.

5. Conclusions

This work has combined hardness and electrical conductivity measurements, TEM observations, and APT experiments for studying a 6101 Al-0.54Mg-0.38Si at.% conductor alloy subjected to two different TMP routes. It was shown that a combination of PA, 50% thickness reduction by CR, and subsequent re-ageing caused a considerable improvement in conductivity (2 – 3%IACS) over conventional isothermal ageing after equal ageing times. APT experiments showed that the difference in conductivity could largely be explained based on the increased solute depletion of the Al matrix in the deformed and re-aged material, as compared to the undeformed material. The conductivity of the deformed material developed in two main stages after re-ageing. At the beginning of re-ageing there occurred a rapid increase in conductivity, which was proposed to occur due to pipe diffusion of solutes along the entangled dislocation network, effectively 'vacuuming' the matrix of solutes. After 2 h re-ageing, the rate of change in conductivity was nearly equal in the deformed and underformed materials, and this subsequent stage is characterised by conventional overageing behaviour, with coarsening of larger precipitates and dissolution of smaller ones. TEM observations of the deformed and undeformed materials showed that there were differences with respect to the resulting distribution of precipitate phases that formed with ageing. Most strikingly, the precipitate distribution in the deformed material became progressively more inhomogeneous with ageing, and showed clear interactions with the dislocation microstructure.

The improved understanding of the effect of unconventional materials processing on the resulting microstructure and its link to conductivity increase has important implications for future alloy developments. The insights gained should help in designing new alloy processing routines that may achieve progressively better combinations of high conductivity and strength in Al alloys, which are normally mutually exclusive properties in metallic systems.

Data availability

The raw/processed data required to reproduce these findings cannot be shared at this time due to technical limitations but can be made available upon reasonable request.

Declaration of Competing Interest

The authors declare that they have no known competing financial interests or personal relationships that could have appeared to influence the work reported in this paper.

Acknowledgements

All authors acknowledge support from the AMPERE project (NFR 247783), a knowledge building project for industry, co-financed by The Research Council of Norway (NFR), and the industrial partners Hydro, Gränges, Neuman Aluminium Raufoss (Raufoss Technology), and Nexans. The (S)TEM work was performed using the NORTEM infrastructure (NFR 197405) at the TEM Gemini Centre, Trondheim, Norway.

References

[1] F. Kiessling, P. Nefzger, J.F. Nolasco, U. Kaintzyk, Overhead Power Lines, 1st edition, Springer-Verlag, Berlin Heidelberg, 2003.
[2] S. Karabay, Modification of AA-6201 alloy for manufacturing of high conductivity and extra high conductivity wires with property of high tensile stress after artificial aging heat treatment for all-aluminium alloy conductors, Mater. Des. 27 (10) (2006) 821–832.
[3] S. Karabay, Influence of AlB2 compound on elimination of incoherent precipitation in artificial aging of wires drawn from redraw rod extruded from billets cast of alloy AA-6101 by vertical direct chill casting, Mater. Des. 29 (7) (2008) 1364–1375.
[4] X. Sauvage, E.V. Bobruk, M.Yu. Murashkin, Y. Nasedkina, N.A. Enikeev, R. Z. Valiev, Optimization of electrical conductivity and strength combination by structure design at the nanoscale in Al-mg-Si alloys, Acta Mater. 98 (2015) 355–366.
[5] G.A. Edwards, K. Stiller, G.L. Dunlop, M.J. Couper, The precipitation sequence in Al–Mg–Si alloys, Acta Mater. 46 (11) (1998) 3893–3904.
[6] C.D. Marioara, S.J. Andersen, H.W. Zandbergen, R. Holmestad, The influence of alloy composition on precipitates of the Al-Mg-Si system, Metall. Mater. Trans. A 36 (13) (2005) 691–702.
[7] H.S. Hasting, A.G. Frøseth, S.J. Andersen, R. Vissers, J.C. Walmsley, C.D. Marioara, F. Danoix, W. Lefebvre, R. Holmestad, Composition of β'' precipitates in Al–Mg–Si alloys by atom probe tomography and first principles calculations, J. Appl. Phys. 106 (12) (dec 2009).
[8] R. Vissers, M.A. van Huis, J. Jansen, H.W. Zandbergen, C.D. Marioara, S. J. Andersen, The crystal structure of the β' phase in Al–Mg–Si alloys, Acta Mater. 55 (11) (jun 2007) 3815–3823.
[9] S.J. Andersen, C.D. Marioara, R. Vissers, A. Frøseth, H.W. Zandbergen, The structural relation between precipitates in Al-mg-Si alloys, the Al-matrix and diamond silicon, with emphasis on the trigonal phase U1-MgAl2Si2, Mater. Sci. Eng. A 444 (1–2) (2007) 157–169.
[10] S.J. Andersen, C.D. Marioara, A. Frøseth, R. Vissers, H.W. Zandbergen, Crystal structure of the orthorhombic U2-Al4Mg4Si4 precipitate in the Al–Mg–Si alloy system and its relation to the β' and β'' phases, Mater. Sci. Eng. A 390 (1–2) (jan 2005) 127–138.
[11] S.D. Dumolt, D.E. Laughlin, J.C. Williams, Formation of a modified β' phase in aluminum alloy 6061, Scr. Metall. 18 (12) (1984) 1347–1350.
[12] A.H. Geisler, J.K. Hill, Analyses and interpretations of X-ray diffraction effects in patterns of aged alloys, Acta Crystallogr. 1 (5) (1948) 238–252.
[13] M. Yu Murashkin, I. Sabirov, V.U. Kazykhanov, E.V. Bobruk, A.A. Dubravina, R. Z. Valiev, Enhanced mechanical properties and electrical conductivity in ultrafine-grained Al alloy processed via ECAP-PC, J. Mater. Sci. 48 (13, SI) (2013) 4501–4509.
[14] M. Murashkin, A. Medvedev, V. Kazykhanov, A. Krokhin, G. Raab, N. Enikeev, R. Z. Valiev, Enhanced mechanical properties and electrical conductivity in ultrafine-grained Al 6101 alloy processed via ECAP-conform, Metals 5 (4) (2015) 2148–2164.
[15] K. Majchrowicz, Z. Pakiela, W. Chrominski, M. Kulczyk, Enhanced strength and electrical conductivity of ultrafine-grained Al-mg-Si alloy processed by hydrostatic extrusion, Mater. Charact. 135 (2018) 104–114.
[16] J.P. Hou, Q. Wang, Z.J. Zhang, Y.Z. Tian, X.M. Wu, H.J. Yang, X.W. Li, Z.F. Zhang, Nano-scale precipitates: the key to high strength and high conductivity in Al alloy wire, Mater. Des. 132 (2017) 148–157.
[17] C.H. Liu, J. Chen, Y.X. Lai, D.H. Zhu, Y. Gu, J.H. Chen, Enhancing electrical conductivity and strength in Al alloys by modification of conventional thermo-mechanical process, Mater. Des. 87 (2015) 1–5.
[18] G. Lin, Z. Zhang, H. Wang, K. Zhou, Y. Wei, Enhanced strength and electrical conductivity of Al-Mg-Si alloy by thermo-mechanical treatment, Mater. Sci. Eng. A 650 (2016) 210–217.
[19] D.J. Larson, T.J. Prosa, R.M. Ulfig, B.P. Geiser, T.F. Kelly, Local Electrode Atom Probe Tomography, Springer, New York, 2013.
[20] S.J. Andersen, Quantification of the Mg2Si β'' and β' phases in AlMgSi alloys by transmission electron microscopy, Metall. Mat.Transac. A 26 (8) (1995) 1931–1937.
[21] E. Christiansen, C.D. Marioara, B. Holmedal, O.S. Hopperstad, R. Holmestad, Nano-scale characterisation of sheared β'' precipitates in a deformed aluminium alloy, Sci. Rep. 9 (1) (2019) 17446.
[22] M.H. Mulazimoglu, R. Drew, J.E. Gruzelski, Electrical-conductivity of aluminum-rich Al-Si-Mg alloys, J. Mater. Sci. Lett. 8 (3) (1989) 297–300.
[23] F.R. Fickett, Aluminum—1. A review of resistive mechanisms in aluminum, Cryogenics 11 (5) (1971) 349–367.
[24] T.S. Orlova, A.M. Mavlyutov, A.S. Bondarenko, I.A. Kasatkin, M.Yu. Murashkin, R. Z. Valiev, Influence of grain boundary state on electrical resistivity of ultrafine grained aluminium, Philos. Mag. 96 (23) (2016) 2429–2444.
[25] Y. Miyajama, S.-Y. Komatsu, M. Mitsuhara, S. Hata, H. Nakashima, N. Tsuji, Change in electrical resistivity of commercial purity aluminium severely plastic deformed, Philos. Mag. 90 (34) (2010) 4475–4488.
[26] Y. Wang, D.J. Srolovitz, J.M. Rickman, R. Lesar, Dislocation motion in the presence of diffusing solutes: a computer simulation study, Acta Mater. 48 (9) (2000) 2163–2175.
[27] M. Militzer, W.P. Sun, J.J. Jonas, Modelling the effect of deformation-induced vacancies on segregation and precipitation, Acta Metall. Mater. 42 (1) (1994) 133–141.
[28] M.J. Zehetbauer, G. Steiner, E. Schafler, A. Korznikov, E. Korznikova, Deformation induced vacancies with severe plastic deformation: Measurements and modelling, in: Z. Horita (Ed.), Nanomaterials by severe plastic deformation, volume 503–504 of Materials Science Forum, 2006, pp. 57–64.
[29] E. Thronsen, C.D. Marioara, J.K. Sunde, K. Minakuchi, T. Katsumi, I. Erga, S. J. Andersen, J. Friis, K. Marthinsen, K. Matsuda, R. Holmestad, The effect of heavy deformation on the precipitation in an Al-1.3Cu-1.0Mg-0.4Si wt.% alloy, Mater. Des. 186 (2020) 108203.

[30] N. Louat, On the theory of the Portevin-Le Chateriler effect, Scr. Metall. 15 (11) (1981) 1167–1170.
[31] W.A. Curtin, D.L. Olmsted, L.G. Hector Jr., A predictive mechanism for dynamic strain ageing in aluminium-magnesium alloys, Nat. Mater. 5 (11) (2006) 875–880.
[32] G.P.M. Leyson, W.A. Curtin, L.G. Hector Jr., C.F. Woodward, Quantitative prediction of solute strengthening in aluminium alloys, Nat. Mater. 9 (9) (2010) 750–755.
[33] G.R. Love, Dislocation pipe diffusion, Acta Metall. 12 (6) (1964) 731.
[34] J. Mimkes, Pipe diffusion along isolated dislocations, Thin Solid Films 25 (1) (1975) 221–230.
[35] R.W. Balluffi, On measurements of self-diffusion rates along dislocations in f.c.c. metals, Phys. Status Solidi B 42 (1) (1970) 11–34.
[36] G.P. Purja Pun, Y. Mishin, A molecular dynamics study of self-diffusion in the cores of screw and edge dislocations in aluminum, Acta Mater. 57 (18) (2009) 5531–5542.
[37] R.C. Picu, D. Zhang, Atomistic study of pipe diffusion in Al-Mg alloys, Acta Mater. 52 (1) (2004) 161–171.
[38] M. Legros, G. Dehm, E. Arzt, T.J. Balk, Observation of giant diffusivity along dislocation cores, Science 319 (5870) (2008) 1646–1649.
[39] T.E. Volin, K.H. Lie, R.W. Balluffi, Measurement of rapid mass transport along individual dislocations in aluminum, Acta Metall. 19 (4) (1971) 263–274.
[40] A. Varschavsky, E. Donoso, A calorimetric investigation on the kinetics of solute segregation to partial dislocations in Cu–3.34at%Sn, Mater. Sci. Eng. A 251 (1) (1998) 208–215.